UC Berkeley
UC Berkeley Previously Published Works

Title
Theoretical Investigation of the Activity of Cobalt Oxides for the Electrochemical Oxidation of Water

Permalink
https://escholarship.org/uc/item/7bx525z3

Journal
Journal of the American Chemical Society, 135(36)

ISSN
0002-7863

Authors
Bajdich, Michal
García-Mota, Mónica
Vojvodic, Aleksandra
et al.

Publication Date
2013-09-11

DOI
10.1021/ja405997s

Peer reviewed

eScholarship.org Powered by the California Digital Library
University of California

JACS
JOURNAL OF THE AMERICAN CHEMICAL SOCIETY
Article
pubs.acs.org/JACS

Theoretical Investigation of the Activity of Cobalt Oxides for the Electrochemical Oxidation of Water

Michal Bajdich,[†,§] Mónica García-Mota,[‡] Aleksandra Vojvodic,[‡] Jens K. Nørskov,*[,‡] and Alexis T. Bell*[,†,§]

[†]The Joint Center for Artificial Photosynthesis, Lawrence Berkeley National Laboratory, Berkeley, California 94720, United States

[‡]SUNCAT Center for Interface Science and Catalysis, Department of Chemical Engineering, Stanford University, Stanford, California 94305, United States

[§]Department of Chemical and Biomolecular Engineering, University of California at Berkeley, Berkeley, California 94720, United States

Supporting Information

ABSTRACT: The presence of layered cobalt oxides has been identified experimentally in Co-based anodes under oxygen-evolving conditions. In this work, we report the results of theoretical investigations of the relative stability of layered and spinel bulk phases of Co oxides, as well as the stability of selected surfaces as a function of applied potential and pH. We then study the oxygen evolution reaction (OER) on these surfaces and obtain activity trends at experimentally relevant electro-chemical conditions. Our calculated volume Pourbaix diagram shows that β-CoOOH is the active phase where the OER occurs in alkaline media. We calculate relative surface stabilities and adsorbate coverages of the most stable low-index surfaces of β-CoOOH: (0001), (01$\bar{1}$2), and (10$\bar{1}$4). We find that at low applied potentials, the (10$\bar{1}$4) surface is the most stable, while the (01$\bar{1}$2) surface is the more stable at higher potentials. Next, we compare the theoretical overpotentials for all three surfaces and find that the (10$\bar{1}$4) surface is the most active one as characterized by an overpotential of η = 0.48 V. The high activity of the (10$\bar{1}$4) surface can be attributed to the observation that the resting state of Co in the active site is Co^{3+} during the OER, whereas Co is in the Co^{4+} state in the less active surfaces. Lastly, we demonstrate that the overpotential of the (10$\bar{1}$4) surface can be lowered further by surface substitution of Co by Ni. This finding could explain the experimentally observed enhancement in the OER activity of $Ni_yCo_{1-y}O_x$ thin films with increasing Ni content. All energetics in this work were obtained from density functional theory using the Hubbard-U correction.

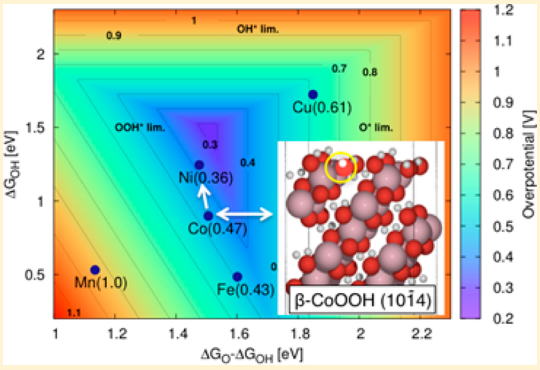

1. INTRODUCTION

The electrochemical splitting of water offers an attractive means for providing a carbon-free source of hydrogen when the necessary energy is provided by solar radiation. The overall process of water splitting comprises two half reactions: the evolution of O_2 and the evolution of H_2. Extensive research on this subject[1,2] has shown that the potential needed to split water at rates provided by the solar flux (e.g., 10 mA/cm^2) is limited primarily by the oxygen evolution reaction (OER), since none of the currently known catalysts for this reaction have an overpotential that is less than ~230 mV at the above rate.[3] Thus, an important challenge is the discovery and development of OER catalysts that can reduce the overpotential for the OER. Moreover, for practical reasons the catalyst must be based on earth-abundant materials.[1,2] Past work has shown that a reasonable starting point is the oxides of Ni and Co, since these materials have been shown to perform well and to be stable in alkaline electrolytes.[4]

In the present study we have focused on understanding the factors influencing the performance of Co oxides and identifying means for improving their performance. Several recent studies have shown that in alkaline electrolyte Co_3O_4 undergoes oxidation to CoOOH via the reaction[5] $Co_3O_4 + OH^- + H_2O \rightarrow 3CoOOH + e^-$ as the potential is raised to the onset of the OER and that CoOOH is the bulk phase present during evolution of O_2.[6−8] While it is known that surface morphology can affect the activity of catalysts in general and that adsorbed species can further alter the surface structure of the active catalysts, the way in which these effects affect the activity of electrocatalysts for the OER is not fully understood. In the present study we address these questions by carrying out a theoretical investigation to identify the effects of electrolyte pH and applied potential on the most thermodynamically stable bulk and surface phases of Co oxides and to estimate the influence of these variables on the overpotential for the OER.

Theoretical investigations of the OER have been carried out for metals[9] and metal oxides with a rutile structure.[10] The rutile phase of TiO_2 has received particular attention[11−13] because of its potential as a photocatalyst. More recent work has focused

Received: June 14, 2013
Published: August 14, 2013

 © 2013 American Chemical Society dx.doi.org/10.1021/ja405997s | J. Am. Chem. Soc. 2013, 135, 13521−13530

on transition metal oxides[14,15] with rutile, anatase, and perovskite structures, as well as spinel-type oxides. The effects of doping metal oxides by other transition metal cations have also been reported. For example, it has been found theoretically that increases in the OER activity of the (0001) surface of hematite can be improved by Ni and Co doping[16] and the activity of the (110) surface of rutile TiO_2 can be improved by Mn and Mo doping.[17] It is noted that the majority of the studies have been conducted at the generalized-gradient approximation (GGA) level of density functional theory (DFT). We have recently reported that inclusion of the Hubbard-U correction (i.e., GGA+U) leads to improvement of the description of the OER activity of Co_3O_4 and CoOOH.[18]

In the present study we have used DFT at the GGA+U level to determine the relative stability of bulk $Co(OH)_2$, Co_3O_4 (spinel phase), CoOOH, and CoO_2 via the Pourbaix method. All of these phases, with the exception of spinel, are composed of CoO_2 layers in edge-sharing octahedral geometry with 2, 1, or 0 interlayer hydrogen(s) per CoO_2 unit. We then focus on the low-index surfaces of CoOOH, which has been identified as the active phase, and study the influence of pH and applied potential on the surface structure of this compound. The theoretical overpotential for the OER is then determined for these low-index surfaces. No consideration was given, though, to non-stoichiometric CoOOH.[19] Lastly, we investigated the effect of doping the surface of CoOOH by first row transition metal cations on the overpotential for the OER.

2. THEORETICAL APPROACH

Thermodynamics of Water Oxidation. The thermodynamic potential for the oxidation of water to produce oxygen, $2H_2O \rightarrow O_2 + 4H^+ + 4e^-$, is 1.23 V at standard conditions (T = 298.15 K, P = 1 bar, pH = 0). In practice, though, a potential above 1.23 V is required in order for this reaction to proceed at a measurable rate. For heterogeneous catalysts, this additional potential is referred to as the overpotential η.

With the exception of IrO_2, all heterogeneous OER catalysts including Co oxides operate in alkaline conditions. The elementary steps by which the OER occurs are believed to involve adsorbed OH and O species on the surface (*) according to the following scheme:

$$OH^- + * \rightarrow OH^* + e^- \quad (1)$$

$$OH^* + OH^- \rightarrow O^* + H_2O + e^- \quad (2)$$

where O_2 is thought to form via one of two pathways. The first pathway involves direct recombination of two O* intermediates as

$$O^* + O^* \rightarrow O_2 \quad (3)$$

and the second pathway involves the reaction of O* with OH^- in a two-step sequence that proceeds via OOH* as an intermediate according to

$$O^* + OH^- \rightarrow OOH^* + e^- \quad (4)$$

$$OOH^* + OH^- \rightarrow O_2 + H_2O + e^- \quad (5)$$

Only reactions 4 and 5 will be considered hereafter, since the thermodynamic barrier for reaction 3 is almost always larger (see refs 15 and 20 for a detailed discussion).

To model the thermochemistry of the OER, it is more convenient to work at acidic conditions, where steps 1, 2, 4, and 5 are modified as

$$2H_2O + * \rightarrow OH^* + H_2O + e^- + H^+ \quad (6)$$

$$OH^* + H_2O \rightarrow O^* + H_2O + e^- + H^+ \quad (7)$$

$$O^* + H_2O \rightarrow OOH^* + e^- + H^+ \quad (8)$$

$$OOH^* \rightarrow O_2 + e^- + H^+ \quad (9)$$

The two schemes (reactions 1, 2, 4, and 5 and reactions 6−9) are equivalent from a thermodynamic perspective. At neutral pH, substitution of $H_2O(l) \rightleftharpoons H^+(aq) + OH^-(aq)$ into the first scheme naturally leads to the second scheme.

The Gibbs free energy change for steps 6−9 can be expressed as

$$\Delta G_1 = \Delta G_{OH} - eU + \Delta G_{H+}(pH) \quad (10)$$

$$\Delta G_2 = \Delta G_O - \Delta G_{OH} - eU + \Delta G_{H+}(pH) \quad (11)$$

$$\Delta G_3 = \Delta G_{OOH} - \Delta G_O - eU + \Delta G_{H+}(pH) \quad (12)$$

$$\Delta G_4 = 4.92\ [eV] - \Delta G_{OOH} - eU + \Delta G_{H+}(pH) \quad (13)$$

where U is the potential measured against normal hydrogen electrode (NHE) at standard conditions (T = 298.15 K, P = 1 bar, pH = 0). The free energy change of the protons relative to the above specified electrode at non-zero pH is represented by Nernst equation as $\Delta G_{H+}(pH) = -k_B T \ln(10) \times pH$. The sum of ΔG_{1-4} is fixed to the negative of experimental Gibbs free energy of formation of two water molecules $-2\Delta g^{exp}_{H2O} = 4 \times 1.23 = 4.92$ eV in order to avoid the calculation of the O_2 bond energy, which is difficult to determine accurately within GGA-DFT. The Gibbs free energies of eqs 10−13 depend on the adsorption energies of OH*, O*, and OOH*. The Gibbs free energy differences of these intermediates include zero point energy (ZPE) and entropy corrections (listed in Supplementary Table S1) according to $\Delta G_i = \Delta E_i + \Delta ZPE_i - T\Delta S_i$ and energy differences ΔE_i calculated relative to H_2O and H_2 (at U = 0 and pH = 0) as

$$\Delta E_{OH} = E(OH^*) - E(*) - [E(H_2O) - \frac{1}{2}E(H_2)] \quad (14)$$

$$\Delta E_O = E(O^*) - E(*) - [E(H_2O) - E(H_2)] \quad (15)$$

$$\Delta E_{OOH} = E(OOH^*) - E(*) - [2E(H_2O) - \frac{3}{2}E(H_2)] \quad (16)$$

The theoretical overpotential is then readily defined as:

$$\eta = \max[\Delta G_1, \Delta G_2, \Delta G_3, \Delta G_4,]/e - 1.23\ [V] \quad (17)$$

We note that the overpotential given by eq 17 is only a thermodynamic quantity, but it has been found to scale well with measured overpotentials, which depend on the concentration of active sites and the current density.[21]

Computational Methodology. All components of free energies were obtained within the GGA-DFT plus Hubbard-U framework (GGA+U),[22−24] which has been shown to improve the description of bulk oxidation energies,[25] formation energies,[26] surface energies,[27,28] and redox potentials[29] of transition metal oxides. This approach has also been shown to be more accurate for predicting the theoretical overpotentials for the OER occurring on Co oxides.[18] All calculations were performed with the GPAW code[30] using the ASE simulation package.[31] The inner cores of the atoms were replaced by all-electron, frozen-core,

Table 1. Measured and Calculated Lattice Constants for Layered and Spinel Co Oxides[a]

compound	space group	structure	a_{hex}/c_{hex} (exp)[ref] [Å]	a_{hex}/c_{hex} (calc) [Å]	ΔG°_f (exp) [eV/fu]	ΔG°_f (calc) [eV/fu]	ground state/moment [μ_B]
β-$Co(OH)_2$	$P\bar{3}m1$	layered-P2	3.182[54]	3.262	−4.77	−5.00	AFM, high-spin, 2.84
			4.658	4.891	−4.73[55]		
β-CoOOH	$R\bar{3}m$	layered-P3	2.851[56,57]	2.922	−4.00[58]	−3.98	PM, low spin, ∼0
			13.150	13.150	−3.72[55]		
CoO	$Fm\bar{3}m$	rocksalt	4.263[59]	4.372	−2.22[60]	−2.10	AFM, high-spin, 2.72
			4 units				
Co_3O_4	$Fd\bar{3}m$	spinel	8.08[61]	8.244	−8.24[40]	−8.34	AFM, Co^{2+}: high-spin 2.65 Co^{3+}: low-spin, ∼0
			8 units		−7.28[55]		
CoO_2	$P\bar{3}m1$	layered-O1	2.822[62]	2.87	−2.25[55]	−2.37	AFM, low-spin 1.23
			4.29	4.144			

[a]The letters O and P are used to designate octahedral and prismatic cation coordination, respectively; and the digit following P or O indicates the number of primitive CoO_2 layers. The labels PM (paramagnetic) and AFM (anti-ferromagnetic) refer to the atomic spin configurations of Co.

projector augmented-wave potentials (PAW),[32] and the electronic wave functions were represented on a uniform real-spaced grid.[30]

The rotationally invariant implementation of Hubbard-U model by Dudarev[33] was employed with the revised Perdew−Burke−Ernzerhof exchange-correlation functional (RPBE)[34] and applied to the 3d electrons of Co atoms and dopants. Following the approach of Wang and Ceder,[25] the effective Hubbard-U parameter (U-J) was fitted to recover the experimental oxidation energy for the reaction $6CoO + O_2 \rightarrow 2Co_3O_4$. The value of (U-J) equal to U_{eff} = 3.52 eV, reported in our previous work,[18] in good agreement with values reported by others,[25,26,35] was used throughout this work. In principle, the U_{eff} value could also be calculated from linear response[36] or in connection with unrestricted Hartree−Fock theory.[37] Using the latter approach, it was found in ref 25 that the U_{eff} values are close to the empirical estimates of Wang and Ceder.

Bulk Properties. For accurate prediction of bulk properties, the lattice constants of each compound, listed in Table 1, were optimized within their respective primitive cell using a finite grid spacing of 0.12 Å and a dense 12 × 12 × 12 Monkhorst−Pack k-point mesh considering ferromagnetic and anti-ferromagnetic ordering. As expected, the GGA+U approach consistently overestimates experimental crystalline lattice constants (by less than 2%, see Table 1), a trend observed previously (see, e.g., ref 38). The calculated lowest energy magnetic structures are consistent with experimental and previously calculated[25] data, with Co^{2+} and Co^{4+} ions having average magnetic moments of 2.75 ± 0.05 μ_B and 1.23 μ_B, respectively (Table 1). Co^{3+} ions were always found to be in their non-magnetic state.

The formation free energies, ΔG°_f, were calculated within the GGA and GGA+U mixing scheme of Jain et al.,[26] using the spinel Co_3O_4 and rocksalt CoO experimental formation enthalpies as references. Next, following above scheme, the chemical potential for oxygen was chosen to match the experimental enthalpies of simple oxides Li_2O and Na_2O. Using the entropy corrections from Supplementary Table S1, the value obtained using the RPBE functional and our potential for oxygen was μ_O = −4.37 eV. To obtain the reference state for hydrogen, we follow the approach of Persson et al.,[39] with the choice of preserving the Gibbs free energy of formation of water, e.g., $\mu_H = [g_{H2O} - \mu_O - \Delta g^{exp}_{H2O}]/2 \approx [(E^{DFT} - T\Delta S^{exp})_{H2O} - (-4.37) - (-2.46)]/2 = -3.70$ eV, where E^{DFT} and $T\Delta S^{exp}$ of water are listed in Supplementary Table S1. The calculated Gibbs free energies, which do not include entropies of the solid compounds, agree well with the latest experimental data (see Table I and Supplementary Figure S1), with the exception of that for β-$Co(OH)_2$, which is overestimated by $\Delta\mu_s^{exp\text{-}calc}$ = 0.23 eV/fu. To construct the volume Pourbaix diagram, we followed the scheme developed by Persson et al.,[39] with the energies of dissolved states, i.e., the aqueous ions, taken from Chivot et al.[40] and corrected by $-\Delta\mu_s^{exp\text{-}calc}$ for β-$Co(OH)_2$.

Surface Properties. All surface energies were calculated within GGA+U as defined above using a simulation cell size of 2 × 2 primitive cells, i.e., with four Co sites per each surface. A minimal thickness of four Co oxide layers with 15 Å of vacuum was required to obtain convergence in the adsorption energies and to recover the bulk magnetic ordering of the center layers. For computational efficiency, a larger grid spacing of 0.2 Å and sparser 3 × 3 × 1 k-point sampling was used for all surface properties. This choice affects the calculated energy differences by less than 0.05 eV, as we have established previously.[18] The surface Pourbaix diagrams and adsorption energies of intermediates were calculated from eqs 10−13 on either stoichiometric or non-symmetric slabs for which the two topmost Co oxide layers were allowed to relax below the maximum force threshold of 0.05 eV/Å. A dipole moment correction was used to correct for residual dipole moments perpendicular to the surface. It should be noted that the reported surface energies are based on calculations of the fully relaxed symmetric slabs with five Co oxide layers and near-zero residual dipole moments.

To determine the surface coverage and relative surface stability between different surfaces as a function of applied voltage U and pH, we determined the chemical potentials μ_i of the adsorbed species. For OER, the chemical potentials are the free energies of adsorbents taken relative to the free energy of liquid water and hydrogen gas, written explicitly as functions of pH and applied potential U:

$$\mu_O = [G(H_2O) - G(H_2)] + 2[eU - \Delta G_{H+}(pH)] \quad (18)$$

$$\mu_{OH} = [G(H_2O) - \frac{1}{2}G(H_2)] + [eU - \Delta G_{H+}(pH)] \quad (19)$$

$$\mu_{OOH} = [2G(H_2O) - \frac{3}{2}G(H_2)] + [eU - \Delta G_{H+}(pH)] \quad (20)$$

$$\mu_{H2O} = G(H_2O) \quad (21)$$

dx.doi.org/10.1021/ja405997s | J. Am. Chem. Soc. 2013, 135, 13521−13530

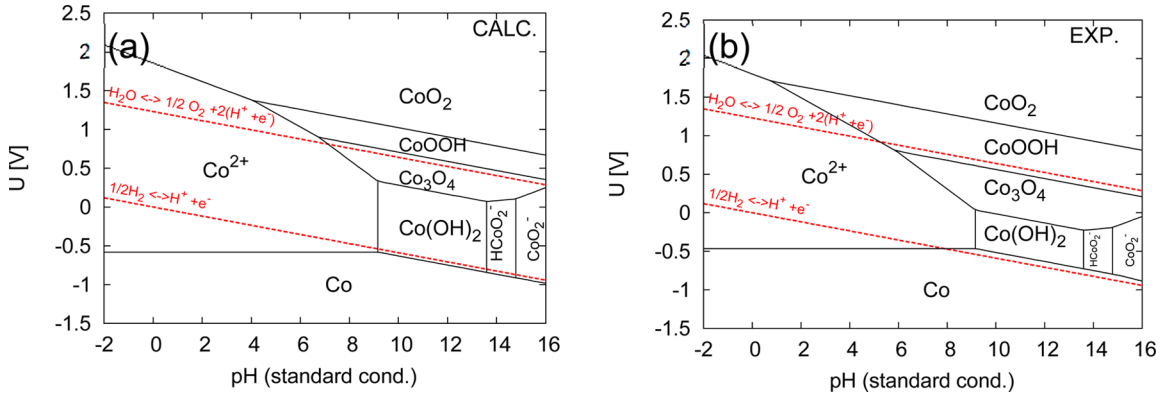

Figure 1. Pourbaix diagrams of bulk phases based on (a) the calculated formation free energies of solid compounds from Table 1 and corrected experimental free energies of aqueous ions of Chivot et al.[39] and (b) based only on experimental formation free energies of Chivot et al. The assumed concentration of Co was fixed at 10^{-6} mol kg^{-1}.

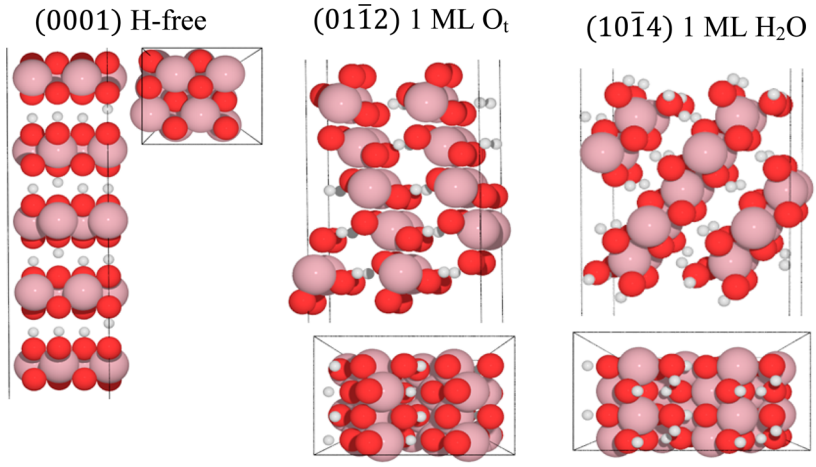

Figure 2. Side- and top-views of the optimized geometries for the lowest-energy surfaces of β-CoOOH represented as 5-layer symmetric slabs and used to determine the surface energies shown in Figure 3. Small white spheres represent H, red spheres represent O, and large pink spheres represent Co atoms.

$$\mu_H = \frac{G(H_2)}{2} - eU + \Delta G_{H+}(pH) \quad (22)$$

To extract the surface free energies, we followed the work of Reuter and Sheffler,[41] in which the surface energy of a symmetric slab of given area 2A and free energy G_{slab} can be obtained as $\gamma = [G_{slab} - \Sigma_i N_i \mu_i]/2A$, where the sum is over chemical potentials μ_i and the number of atoms N_i of each of the constituent species in a slab. It is often more convenient to express γ as a function of the bulk free energy of formation g_{bulk} (using Co as a reference) as $\gamma = [G_{slab} - N_{Co} g_{bulk} - \Sigma_i (N_i - x_i N_{Co})\mu_i]/2A$, where the last sum is the free energy excess of the adsorbed species over the bulk (x_i being the number of atoms per bulk formula). As a consequence, stoichiometric slabs are always independent of chemical potentials. Further, we neglect the ZPE and entropy corrections for g_{bulk} and G_{slab}, which then become equal to the DFT energies of the bulk E^{DFT}_{bulk} and the surface E^{DFT}_{slab}. The ZPE and entropy corrections are, however, included for excess species, in which case the chemical potentials μ_i are given by eqs 18−22. Finally, the Wulff shape of the particles was generated using the Wulffman program.[42]

3. RESULTS

3.1. Pure Co Oxide. The relative stability of the bulk structures of β-$Co(OH)_2$, Co_3O_4, β-CoOOH, and O1-CoO_2 were calculated and used to construct the Pourbaix diagram shown in Figure 1a. The theoretically determined phase boundaries are in good agreement with the experimental Pourbaix diagram of Chivot et al.,[40] shown in Figure 1b. Only two notable differences are observed: the overestimation of the stability of β-$Co(OH)_2$ and a small shift in the relative stability of Co_3O_4 versus CoOOH from below 1.23 V to just above this potential. Most importantly, the CoOOH phase is found to be the stable phase under typical OER conditions (pH = 12−13 and U > 1.23 to ∼1.7 V vs RHE), in agreement with experimental observation.[6−8]

Since β-CoOOH has been identified as the stable bulk phase under OER conditions,[5−7] we next focused our attention on identifying the effects of pH and applied potential on the most thermodynamically stable surfaces of this material. To this end, we calculated the surface free energies of the (10$\bar{1}$4), (0001), and (01$\bar{1}$2) facets for a variety of surface terminations according to the scheme discussed in the section on Computational Methodology. Detailed surface Pourbaix diagrams are included in the Supporting Information. The choice of the low-index surfaces of β-CoOOH was based on the findings of Kramer and Ceder[43] for the structurally related compound α-$LiCoO_2$. Application of the semiempirical Bravais−Friedel−Donnay−Harker (BFDH) method[44−46] to β-CoOOH also revealed the existence of an additional stable facet: (10$\bar{1}$1). However, upon closer examination, this surface

dx.doi.org/10.1021/ja405997s | J. Am. Chem. Soc. 2013, 135, 13521−13530

was found to be less stable than the three surfaces noted above at conditions relevant to OER.

The surface terminations exhibiting the lowest free energies were as follows: H-free (0001) surface, the $(01\bar{1}2)$ surface with 1 mL of O_t (t denotes the top position), and the $(10\bar{1}4)$ surface with 1 mL of coadsorbed H_2O. The structure of each of these surface terminations is shown in Figure 2. The variation in the surface free energy of each of these surfaces with applied potential is shown in Figure 3a for pH = 0. It is evident from

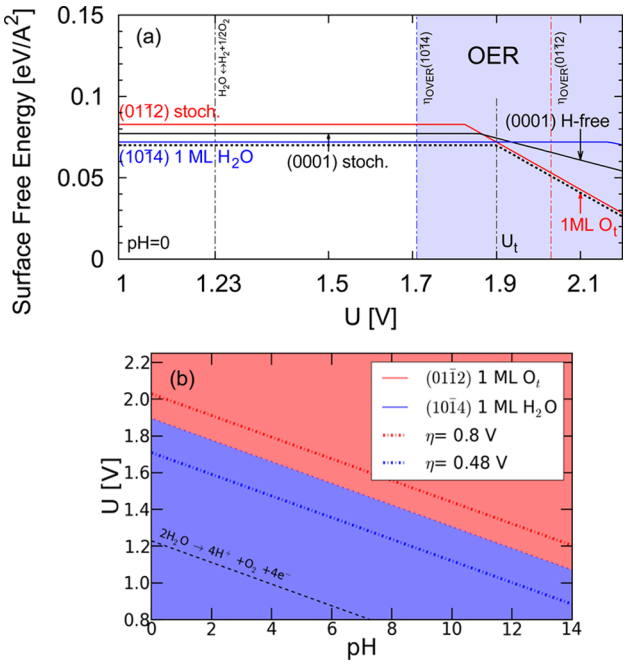

Figure 3. (a) Surface energy of symmetric slabs of β-CoOOH as a function of applied potential at pH = 0. The solid red and black lines indicate the stable terminations of the $(01\bar{1}2)$ and the (0001) surfaces. The solid blue line is for the $(10\bar{1}4)$ surface terminated by 1 mL of H_2O. The black dashed line indicates the overall minimum surface energy. The structures of the relevant surfaces are depicted in Figure 2. The light blue area indicates the region of OER activity. The vertical lines indicate the overpotentials. (b) The transition voltage between the two lowest energy surfaces follows the pH dependence of the reversible-hydrogen electrode, $U_t = 1.90 - 0.059$ pH.

this plot that the $(10\bar{1}4)$ surface with 1 mL of H_2O exhibits the highest stability below the transition voltage of $U_t = 1.90$ V and has a surface energy of 0.072 eV/Å^2. The stability of the $(10\bar{1}4)$ surface is a consequence of the energetically favorable adsorption of H_2O. Above 1.90 V, the $(01\bar{1}2)$ surface terminated with 1 mL of O_t becomes more stable. The value of U_t is pH-dependent, in the same manner as the reversible-hydrogen electrode, and given by $U_t = 1.90 - 0.059$pH, as can be seen in Figure 3b. We note further that the H-free (0001) surface is never the most stable surface in the potential window considered here.

The effect of surface termination for β-CoOOH on the theoretical overpotential of the OER is given in Table 2. The overpotential for the $(10\bar{1}4)$ surface containing 1 mL of adsorbed H_2O is 0.48 V, and the formation of O_2 is thermodynamically limited by the formation of OOH*. By contrast, the overpotential for the $(01\bar{1}2)$ surface with 1 mL of adsorbed O_t is 0.80 V, and the formation of O_2 is limited thermodynamically by the formation of OH*. These results clearly demonstrate that

Table 2. Computed Adsorption Energies Based on Equations 14−16 and Overpotentials for the Surfaces of β-CoOOH

surface	ΔE_{OH} [eV]	ΔE_O [eV]	ΔE_{OOH} [eV]	η [V]
$(01\bar{1}2)$	1.59	3.77	4.35	0.80
$(10\bar{1}4)$	0.47	2.31	3.58	0.48
(0001)	−0.15	1.70	3.29	0.80

for applied potentials below U_t the β-CoOOH$(10\bar{1}4)$ surface terminated with 1 mL of H_2O is the most active surface for the OER. The H-free (0001) surface was found to have overpotential of 0.8 V, with the oxygen evolution limited thermodynamically by the formation of OOH*.

In practice cobalt oxide is most likely to consist of particles, rather than single crystal, and therefore we used the Wulff construction[47] to determine the equilibrium crystal shapes for β-CoOOH particles as function of applied voltage. The results are shown in Figure 4 for pH = 13 (the experimental value of

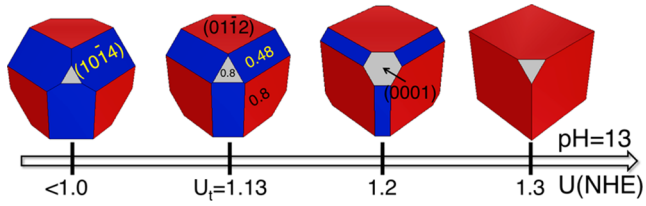

Figure 4. Equilibrium crystal shapes of β-CoOOH determined by Wulff constructions using the surface free energies of Figure 3 at pH = 13. Symbols indicate the surface termination, and small numbers the corresponding theoretical overpotentials. The shape below 1 V stays fixed. At this pH, the transition voltage is $U_t = 1.13$ V, below which only the $(10\bar{1}4)$ surface is active. The surface energies at $U_t = 1.13$ V and pH = 13 used to construct the Wulff shape were 0.0720, 0.0724, and 0.0746 eV/Å^2 for $(10\bar{1}4)$, $(01\bar{1}2)$, and (0001), respectively.

ref 7) and indicate that for low potentials the ratio between the $(10\bar{1}4)$ and the $(01\bar{1}2)$ surface areas is about 1:1, whereas the $(01\bar{1}2)$ surface dominates at higher potentials. These calculations reveal that the observed activity of β-CoOOH particles will depend on the distribution of surface facets, which is a function of the pH and applied potential.

To understand the reasons for the much lower overpotential of the $(10\bar{1}4)$ relative to $(01\bar{1}2)$ surface, it is useful to determine the Bader charges, q, and the local magnetic moments, m, of the Co site participating in the OER at each step of the reaction (see Figures 5 and 6). The values for q and m, given in Table 3, reveal that the Co site can be in only one of three states: (a) $q = 1.36$, $|m| = 2.67$ μ_B, (b) $q = 1.44(\pm 0.02)$, $|m| = 0.0(\pm 0.1)$ μ_B; and (c) $q = 1.57(\pm 0.01)$, $|m| = 1.10(\pm 0.03)$ μ_B, the parentheses indicating the variation in the values within the table. We notice a monotonic increase in the value of q proceeding from (a) to (c). Next, we assign the state of the active site in the OER mechanism. Ligand-field theory predicts that a Co^{2+} site of octahedral symmetry can be either in a high-spin state ($S = 3/2$) or a low-spin state ($S = 1/2$), a Co^{3+} can be in a singlet spin state ($S = 0$), and a Co^{4+} can be in a low-spin state ($S = 1/2$). Similarly, our calculated GGA+U magnetic ground states of compounds (Table 1) have magnetic moments of ~2.7 for Co^{2+}, ~0 for Co^{3+}, and ~1.23 for Co^{4+}. Therefore, we can assign the state of the active site in the mechanism of the OER to have (a) Co^{2+}, (b) Co^{3+}, and (c) Co^{4+} character, respectively.

dx.doi.org/10.1021/ja405997s | J. Am. Chem. Soc. 2013, 135, 13521−13530

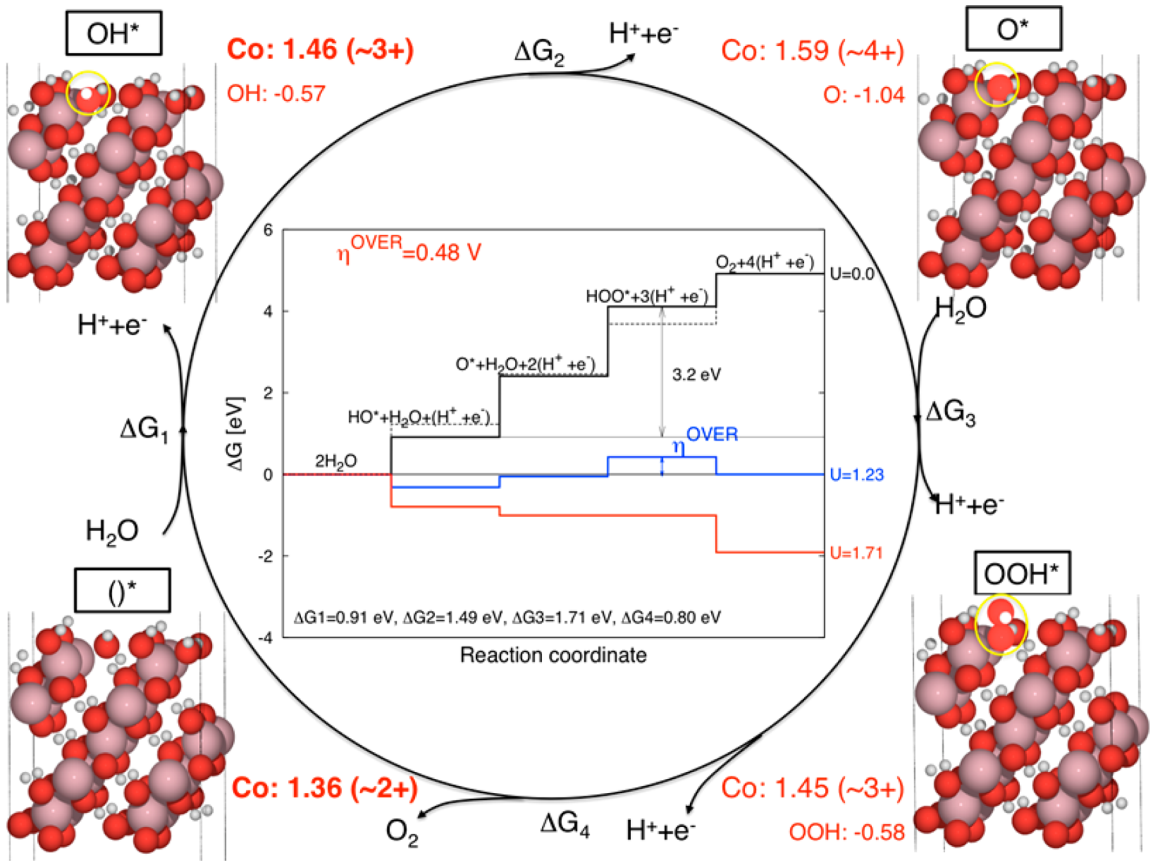

Figure 5. Schematic of the OER on the $(10\bar{1}4)$ surface. The inset shows the free-energy landscape compared to an ideal catalyst (dashed-line) for zero pH. Reaction 3 is the potential-limiting step. For $U > 1.71$ V, all steps are thermodynamically accessible. For each step, we list the measured Bader charge of the Co active site and of the adsorbed species (Table 3).

Table 3. Calculated Bader Charges q (in Units of Electrons) and Local Atomic Magnetic Moments m (in Units of μ_B) for the Co Empty Site As Well As Co Sites Occupied by O, OH, and OOH on the Different Surfaces of β-CoOOH[a]

β-CoOOH	O*			Empty site-(*)		OH*			OOH*		
Surface	q	|m|	q:O	q	|m|	q	|m|	q:OH	q	|m|	q:OOH
$(01\bar{1}2)$	**1.56 (+4)**	**1.07**	**-0.31**	1.48 (+3)	0.03	1.58 (+4)	1.13	-0.25	1.48 (+3)	0.11	-0.14
$(10\bar{1}4)$	1.59 (+4)	1.13	-1.04	1.36 (+2)	2.67	**1.46 (+3)**	**0**	**-0.57**	1.45 (+3)	0.0	-0.58
(0001)	**2×1.57(+4)**	**1.33**	**-0.78**	2×1.45(+3)	0.1	3×1.45 (+3)	0.01	-0.47	3×1.44 (+3)	0.0	-0.46
	1.45(+3)	**0**		1.42(+3)	0.0						

[a]The red bold font indicates the equilibrium state of the surface at OER conditions. The charge character of the active site is indicated in brackets (see also text). For the (0001) surface, the active site is composed of 3 Co atoms.

On the basis of the above assignment, we note that under OER conditions, the $(10\bar{1}4)$ surface is best described as having Co^{3+} ions, while the (0001) and the $(01\bar{1}2)$ the surfaces have more Co^{4+} ions (as indicated by the bold text in Table 3). This is not surprising, since for bulk phases shown in the Pourbaix diagram (Figure 1), higher voltage is needed to achieve higher oxidation states of cobalt. Next, consider the oxidation states of the Co cations during a OER cycle on the $(10\bar{1}4)$ surface (Figure 5) and on the $(01\bar{1}2)$ surface (Figure 6). We notice that the adsorption of OH^- to form OH* involves the oxidation of Co^{2+} to Co^{3+} on the $(10\bar{1}4)$ surface, but a Co^{3+} to Co^{4+} on the $(01\bar{1}2)$ surface. For this step, the Co^{3+} to Co^{4+} transition on the $(01\bar{1}2)$ surface results in a too-weak adsorption and makes the formation of OH* to be the potential-limiting step. For the $(10\bar{1}4)$ surface, on the other hand, the free energy of forming OH* is much closer to the optimal value of 1.23 eV. We note further that the free energies of adsorption for O* and OOH* are also lower for the $(10\bar{1}4)$ surface, since as discussed below, they correlate with that for the formation of OH*, and for this surface the formation of OOH* becomes the potential-limiting step.

3.2. Doped Co Oxide. Previous studies have shown that introduction of transition metal cations into the (110) surface of rutile TiO_2[17] and the (0001) surface of hematite[16] can lead to significant decreases in the theoretical overpotential for the OER. We carried out similar calculations in order to determine the extent to which the overpotential for β-CoOOH could be reduced by substitutional doping of a Co active site by another transition metal cation. To this end, we examined single-site doping of the $(10\bar{1}4)$ and $(01\bar{1}2)$ surfaces as shown in Figures 8 and 9, respectively. The evolution of O_2 is assumed to occur only at the dopant site. These calculations were carried out at

dx.doi.org/10.1021/ja405997s | J. Am. Chem. Soc. 2013, 135, 13521−13530

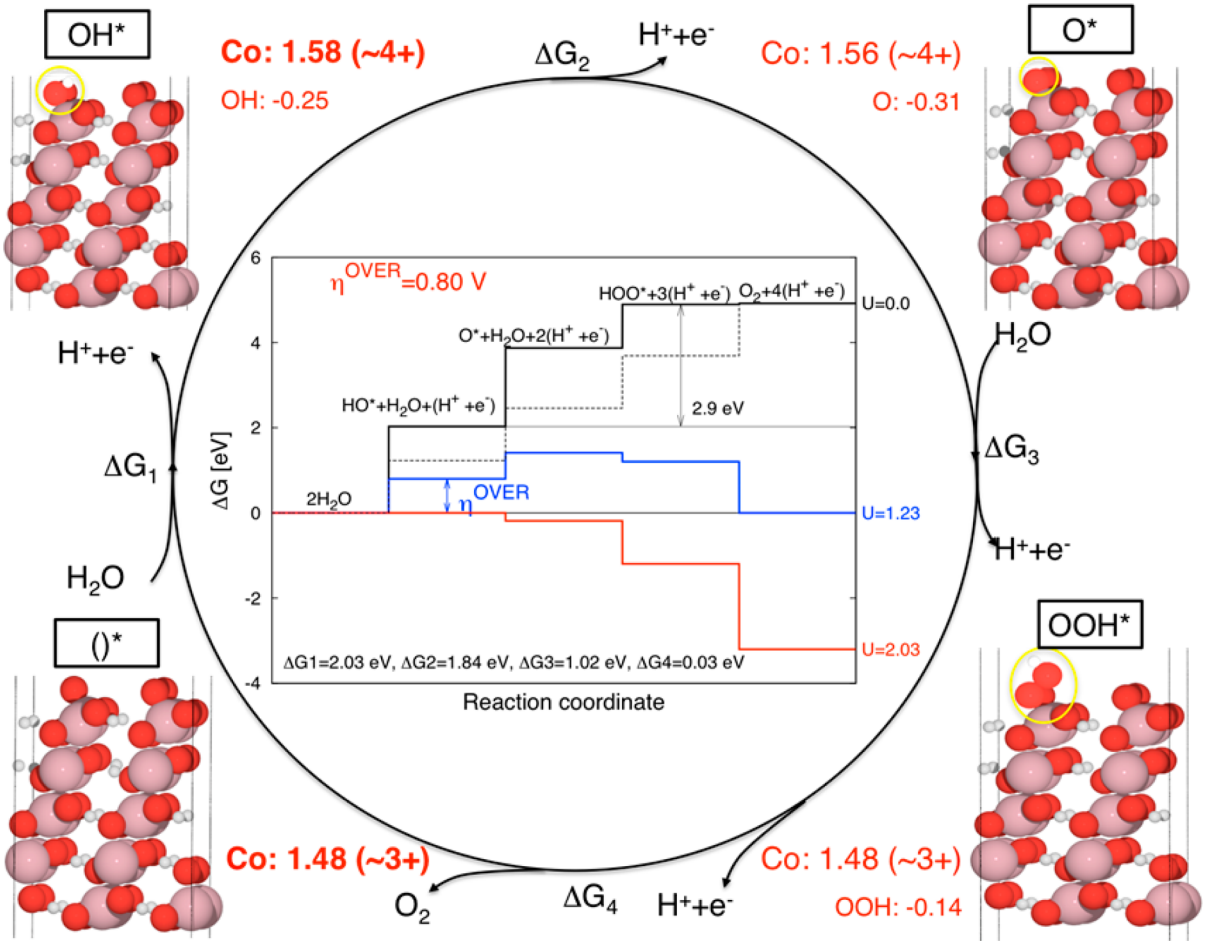

Figure 6. Same as Figure 5 but for the $(01\bar{1}2)$ surface. For this surface, reaction 1 is the potential-limiting step. For $U > 2.03$ V, all steps are thermodynamically accessible. For each step, we list the measured Bader charge of the active Co site and of the adsorbed species (Table 3).

the DFT+U level of theory using a single value of $U_{eff} = 3.52$ eV for all 3d electrons of the dopants and Co atoms, in order to limit the number of free parameters. This approximation is justified by noticing that the values of U_{eff} for Mn, Fe, Co, Ni, and Cu used in other studies[16,25,38] all lie within the narrow range of 3.0−4.3 eV and that variations in U_{eff} for Fe between 3 and 5 eV result in a less than 0.05 V change in the value of η (not shown).

The calculated adsorption energies for both pure and doped surfaces are plotted as scaling relations[9,14,40] between ΔE_O and ΔE_{OH} and between ΔE_{OOH} and ΔE_{OH} in Figure 7a and b, respectively. Figure 7a shows a monotonic weakening in the adsorption energies of all species with increasing number of d electrons of the dopant, and adsorption on the $(10\bar{1}4)$ surface is generally stronger than on the $(01\bar{1}2)$ surface. We find that the scaling relation between ΔE_O and ΔE_{OH} (slope 0.67, intercept 0.96 eV) closely resembles that reported for rutile-type oxides[10] (slope 0.61 and intercept 0.9 eV). The scaling relationship between ΔE_{OH} and ΔE_{OOH} (Figure 7b) also shows above monotonic weakening in the adsorption energies and is compared to approximate universal scaling of $\Delta E_{OOH} = \Delta E_{OH} + (3.2 \pm 0.2)$ eV, observed in rutile oxides and perovskites.[21] However, for the $(10\bar{1}4)$ surface, we find a deviation from this dependence with a smaller slope of 0.69, which is later used for construction of the 2D map of theoretical overpotentials for this surface. We also note that similar reduction in the slope was recently reported by Calle-Vallejo et al. for a variety of metals and metal oxides.[50]

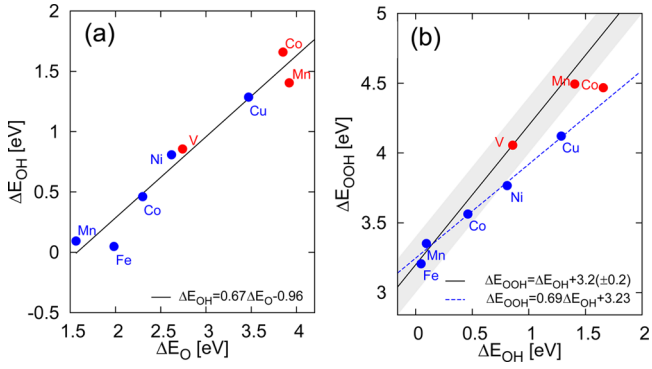

Figure 7. Scaling relations between (a) ΔE_O and ΔE_{OH} and (b) ΔE_{OH} and ΔE_{OOH}. The blue points are for surface doped $(10\bar{1}4)$ and red points for $(01\bar{1}2)$ terminations of β-CoOOH. (a) The scaling between ΔE_O and ΔE_{OH} with single linear fit over data. (b) The scaling between ΔE_{OH} and ΔE_{OOH} with linear fit over only $(10\bar{1}4)$ data (blue dashed line) compared to $\Delta E_{OOH} = \Delta E_{OH} + (3.2 \pm 0.2)$ eV scaling indicated by the shaded area.

The resulting overpotentials for the doped $(10\bar{1}4)$ and $(01\bar{1}2)$ surfaces are plotted on a 2D map of $(\Delta G_O - \Delta G_{OH})$ and ΔG_{OH} energies in Figures 8 and 9. For the $(10\bar{1}4)$ surface (Figure 8), the overpotential for Ni decreases to 0.36 V relative to that for undoped β-CoOOH, 0.48 V. For the $(01\bar{1}2)$ surface (Figure 9), the largest decrease in the overpotential is 0.27 V and occurs for a vanadium dopant, which has an overpotential

dx.doi.org/10.1021/ja405997s | J. Am. Chem. Soc. 2013, 135, 13521−13530

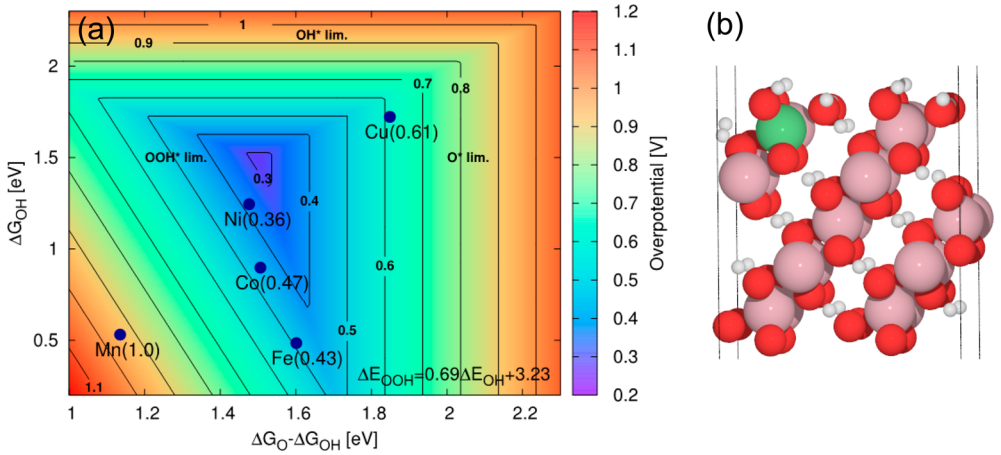

Figure 8. (a) 2D map of theoretical overpotentials η for the doped $(10\bar{1}4)$ surface of β-CoOOH as function of $\Delta G_O - \Delta G_{OH}$ and ΔG_{OH}. The individual values of η are indicated in brackets. The contour map is constructed using fitted scaling of Figure 7b for $(01\bar{1}4)$ points only as $\Delta E_{OOH} = 0.69\Delta E_{OH} + 3.23$ eV in order to minimize the errors in the mapping. Improvement in activity relative to undoped surface is obtained in the case of Ni with $\eta = 0.36$ V and Fe with $\eta = 0.43$ V. (b) The corresponding atomic system with the green sphere indicating a position of the dopant. Only the dopants with $\eta < 1$ V are shown.

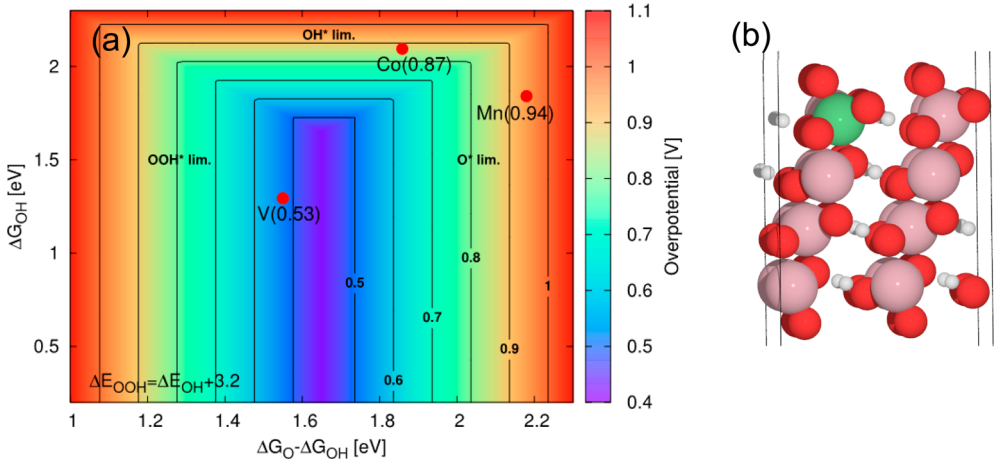

Figure 9. (a) Same as Figure 8, but for the $(01\bar{1}2)$ surface of β-CoOOH. The contour map is constructed assuming $\Delta E_{OOH} = E_{OH} + 3.2$ eV. The improvement relative to undoped surface is obtained in the case of vanadium with $\eta = 0.53$ V. (b) The corresponding atomic system. For computational efficiency, we have reduced the slab to only 4 layers, resulting in a difference of 0.07 V for Co compared to a 5-layer slab. Only the dopants with $\eta < 1$ V are shown.

of 0.53 V compared to the overpotential of 0.8 V for the undoped surface.

It is interesting to examine the results of our work with the recent experimental work of Trotochaud et al.,[51] who report an increase in the OER activity of $Ni_yCo_{1-y}O_x$ thin films with growing Ni content. The measured overpotentials at 1 mA cm^{-2} were $\eta = 380(\pm 10)$ mV for pure CoO_x and $\eta = 341(5)$ mV for $Ni_{0.25}Co_{0.75}O_x$. We note that similar activity enhancement with increasing content of Ni in Ni−Co mixed oxides have also been reported by other investigators when the OER is carried out in alkaline media.[52,53] While the absolute theoretical values of the overpotentials reported here are not directly comparable to experimental values, the observed enhancement in the OER activity upon Ni substitution into CoO_x could in principle be explained by our calculations. As we have shown, the overpotential of the $(10\bar{1}4)$ surface of CoOOH is lowered by 120 mV upon 25% surface doping of Ni (Figure 8). On the other hand, doping of the $(01\bar{1}2)$ surface by Ni leads to no lowering of the overpotential (Figure 9). As we showed above, based on the Wulff construction (see Figure 4) there is a coexistence of the $(10\bar{1}4)$ and the $(01\bar{1}2)$ surfaces with a ratio of approximately 1:1 at the onset of OER. Hence, we can deduce that the activity enhancement of the Ni-doped β-CoOOH$(10\bar{1}4)$ surface, which constitutes about 50% active surface, is responsible for the experimentally observed decrease in the overpotential of 40(±10) mV.

4. CONCLUSIONS

The work presented here has shown that theory at the DFT+U level can be used to predict the bulk and surface structure of cobalt oxide catalysts used for the electrochemical evolution of O_2 under alkaline conditions. The calculated Pourbaix diagram agrees well with the recently reported experimental data. In addition, it predicts β-CoOOH to be the active phase at OER conditions, in agreement with observations by in situ Raman spectroscopy. It is found that the thermodynamically stable surface of β-CoOOH exposed under condition of the OER depends on the pH and the applied potential. Below U_t (U_t = 1.90 V − 0.059pH), the $(10\bar{1}4)$ surface covered by 1 mL of H_2O is the most stable surface, whereas above U_t, the $(01\bar{1}2)$

dx.doi.org/10.1021/ja405997s | J. Am. Chem. Soc. 2013, 135, 13521−13530

surface terminated by 1 mL of O_t is the most stable surface. The theoretical value of the overpotential for the $(10\bar{1}4)$ surface is 0.48 V, and for the $(01\bar{1}2)$ surface it is 0.80 V. Finally, our calculations show that the overpotential for the OER can be reduced to 0.36 V by doping the $(10\bar{1}4)$ surface of β-CoOOH with Ni cations, whereas doping the $(01\bar{1}2)$ surface with V can reduce the overpotential for the OER to 0.53 V. The first of these findings can explain the recently reported enhancement in the activity of $Ni_yCo_{1-y}O_x$ thin films with increasing addition of Ni.

■ ASSOCIATED CONTENT

Supporting Information

Further computational details, components of free energies, Gibbs free energies of formation, and surface Pourbaix diagrams as discussed in the text. This material is available free of charge via the Internet at http://pubs.acs.org.

■ AUTHOR INFORMATION

Corresponding Authors

norskov@stanford.edu
alexbell@berkeley.edu

Notes

The authors declare no competing financial interest.

■ ACKNOWLEDGMENTS

This material is based upon work performed by the Joint Center for Artificial Photosynthesis, a DOE Energy Innovation Hub. The majority of the theoretical work and computer time allocated by the National Energy Research Super Computer (NERSC) was supported through the Office of Science of the U.S. Department of Energy under Award Number DE-SC0004993. Method development and additional computer allocation was provided by the Center of Nanostructuring for Efficient Energy Conversion (CNEEC) at Stanford University, an Energy Frontier Research Center funded by the U.S. Department of Energy, Office of Basic Energy Sciences under Award Number DE-SC0001060. M.B. would like to thank Mary Louie and Yun Cai for useful discussions, Kristin Persson for providing useful contributions regarding the construction of Pourbaix diagrams, and Julien Panetier for careful reading of the manuscript.

■ REFERENCES

(1) Walter, M. G.; Warren, E. L.; McKone, J. R.; Boettcher, S. W.; Mi, Q.; Santori, E. A.; Lewis, N. S. *Chem. Rev.* **2010**, *110*, 6446−6473.
(2) Cook, T. R.; Dogutan, D. K.; Reece, S. Y.; Surendranath, Y.; Teets, T. S.; Nocera, D. G. *Chem. Rev.* **2010**, *110*, 6474−6502.
(3) Matsumoto, Y.; Sato, E. *Mater. Chem. Phys.* **1986**, *14*, 397−426.
(4) Lyons, M. E. G.; Brandon, M. P. *J. Electroanal. Chem.* **2010**, *641*, 119−130.
(5) Hamdani, M.; Singh, R. N.; Chartier, P. *Int. J. Electrochem. Sci.* **2010**, *5*, 556−577.
(6) Kanan, M. W.; Nocera, D. G. *Science* **2008**, *321*, 1072−1075.
(7) Yeo, B. S.; Bell, A. T. *J. Am. Chem. Soc.* **2011**, *133*, 5587−5593.
(8) Subbaraman, R.; Tripkovic, D.; Chang, K.-C.; Strmcnik, D.; Paulikas, A. P.; Hirunsit, P.; Chan, M.; Greeley, J.; Stamenkovic, V.; Markovic, N. M. *Nat. Mater.* **2012**, *11*, 550−557.
(9) Rossmeisl, J.; Logadottir, A.; Nørskov, J. K. *Chem. Phys.* **2005**, *319*, 178−184.
(10) Rossmeisl, J.; Qu, Z.-W.; Zhu, H.; Kroes, G.-J.; Nørskov, J. K. *J. Electroanal. Chem.* **2007**, *607*, 83−89.
(11) Valdés, A.; Qu, Z.-W.; Kroes, G.-J.; Rossmeisl, J.; Nørskov, J. K. *J. Phys. Chem. C* **2008**, *112*, 9872−9879.
(12) Valdés, Á.; Kroes, G.-J. *J. Phys. Chem. C* **2010**, *114*, 1701−1708.
(13) Geng, W. T.; Kim, K. S. *Phys. Rev. B* **2003**, *68*, 125203.
(14) Hansen, H. A.; Man, I. C.; Studt, F.; Abild-Pedersen, F.; Bligaard, T.; Rossmeisl, J. *Phys. Chem. Chem. Phys.* **2009**, *12*, 283−290.
(15) Valdés, Á.; Brillet, J.; Grätzel, M.; Gudmundsdóttir, H.; Hansen, H. A.; Jónsson, H.; Klüpfel, P.; Kroes, G.-J.; Formal, F. L.; Man, I. C.; Martins, R. S.; Nørskov, J. K.; Rossmeisl, J.; Sivula, K.; Vojvodic, A.; Zäch, M. *Phys. Chem. Chem. Phys.* **2011**, *14*, 49−70.
(16) Liao, P.; Keith, J. A.; Carter, E. A. *J. Am. Chem. Soc.* **2012**, *134*, 13296−13309.
(17) García-Mota, M.; Vojvodic, A.; Metiu, H.; Man, I. C.; Su, H.-Y.; Rossmeisl, J.; Nørskov, J. K. *ChemCatChem* **2011**, *3*, 1607−1611.
(18) García-Mota, M.; Bajdich, M.; Viswanathan, V.; Vojvodic, A.; Bell, A. T.; Nørskov, J. K. *J. Phys. Chem. C* **2012**, *116*, 21077−21082.
(19) Bode, H.; Dehmelt, K.; Witte, J. *Electrochim. Acta* **1966**, *11*, 1079−1087.
(20) Nørskov, J. K.; Bligaard, T.; Logadottir, A.; Bahn, S.; Hansen, L. B.; Bollinger, M.; Bengaard, H.; Hammer, B.; Sljivancanin, Z.; Mavrikakis, M.; Xu, Y.; Dahl, S.; Jacobsen, C. J. H. *J. Catal.* **2002**, *209*, 275−278.
(21) Man, I. C.; Su, H.; Calle-Vallejo, F.; Hansen, H. A.; Martínez, J. I.; Inoglu, N. G.; Kitchin, J.; Jaramillo, T. F.; Nørskov, J. K.; Rossmeisl, J. *ChemCatChem* **2011**, *3*, 1159−1165.
(22) Anisimov, V. I.; Aryasetiawan, F.; Lichtenstein, A. I. *J. Phys.: Condens. Matter* **1997**, *9*, 767−808.
(23) Anisimov; Zaanen; Andersen. *Phys. Rev. B* **1991**, *44*, 943−954.
(24) Bacq, O. L.; Pasturel, A.; Bengone, O. *Phys. Rev. B* **2004**, *69*, 245107.
(25) Wang, L.; Maxisch, T.; Ceder, G. *Phys. Rev. B* **2006**, *73*, 195107.
(26) Jain, A.; Hautier, G.; Ong, S. P.; Moore, C. J.; Fischer, C. C.; Persson, K. A.; Ceder, G. *Phys. Rev. B* **2011**, *84*, 045115.
(27) Montoya, A.; Haynes, B. S. *Chem. Phys. Lett.* **2011**, *502*, 63−68.
(28) Chen, J.; Selloni, A. *Phys. Rev. B* **2012**, *85*, 085306.
(29) Zhou, F.; Cococcioni, M.; Marianetti, C. A.; Morgan, D.; Ceder, G. *Phys. Rev. B* **2004**, *70*, 235121.
(30) Enkovaara, J.; Rostgaard, C.; Mortensen, J. J.; Chen, J.; Dułak, M.; Ferrighi, L.; Gavnholt, J.; Glinsvad, C.; Haikola, V.; Hansen, H. A.; Kristoffersen, H. H.; Kuisma, M.; Larsen, A. H.; Lehtovaara, L.; Ljungberg, M.; Lopez-Acevedo, O.; Moses, P. G.; Ojanen, J.; Olsen, T.; Petzold, V.; Romero, N. A.; Stausholm-Møller, J.; Strange, M.; Tritsaris, G. A.; Vanin, M.; Walter, M.; Hammer, B.; Häkkinen, H.; Madsen, G. K. H.; Nieminen, R. M.; Nørskov, J. K.; Puska, M.; Rantala, T. T.; Schiøtz, J.; Thygesen, K. S.; Jacobsen, K. W. *J. Phys.: Condens. Matter* **2010**, *22*, 253202.
(31) Bahn, S. R.; Jacobsen, K. W. *Comp. Sci. Eng.* **2002**, *4*, 56−66.
(32) Kresse, G.; Joubert, D. *Phys. Rev. B* **1999**, *59*, 1758−1775.
(33) Dudarev, S. L.; Botton, G. A.; Savrasov, S. Y.; Humphreys, C. J.; Sutton, A. P. *Phys. Rev. B* **1998**, *57*, 1505−1509.
(34) Hammer, B.; Hansen, L. B.; Nørskov, J. K. *Phys. Rev. B* **1999**, *59*, 7413−7421.
(35) Chen, J.; Wu, X.; Selloni, A. *Phys. Rev. B* **2011**, *83*, 245204.
(36) Cococcioni, M.; de Gironcoli, S. *Phys. Rev. B* **2005**, *71*, 035105.
(37) Mosey, N. J.; Liao, P.; Carter, E. A. *J. Chem. Phys.* **2008**, *129*, 014103−014103−13.
(38) Lutfalla, S.; Shapovalov, V.; Bell, A. T. *J. Chem. Theory Comput.* **2011**, *7*, 2218−2223.
(39) Persson, K. A.; Waldwick, B.; Lazic, P.; Ceder, G. *Phys. Rev. B* **2012**, *85*, 235438.
(40) Chivot, J.; Mendoza, L.; Mansour, C.; Pauporté, T.; Cassir, M. *Corros. Sci.* **2008**, *50*, 62−69.
(41) Reuter, K.; Scheffler, M. *Phys. Rev. B* **2001**, *65*, 035406.
(42) Roosen, A. R.; McCormack, R. P.; Carter, W. C. *Comput. Mater. Sci.* **1998**, *11*, 16−26.
(43) Kramer, D.; Ceder, G. *Chem. Mater.* **2009**, *21*, 3799−3809.
(44) Bravais, A. *Etudes Cristallographiques*; Paris: Gauthier Villars, 1866.
(45) Friedel, G. *Bull. Soc. Fr. Mineral.* **1907**, *30*, 326.
(46) Donnay, J. D. H.; Harker, D. *Am. Mineral.* **1937**, *22*, 463.
(47) Cahn, J. W.; Carter, W. C. *Metall. Mater. Trans. A* **1996**, *27*, 1431−1440.

(48) Calle-Vallejo, F.; Martínez, J. I.; Rossmeisl, J. *Phys. Chem. Chem. Phys.* **2011**, *13*, 15639−15643.
(49) Koper, M. T. M. *J. Electroanal. Chem.* **2011**, *660*, 254−260.
(50) Calle-Vallejo, F.; Inoglu, N. G.; Su, H.-Y.; Martínez, J. I.; Man, I. C.; Koper, M. T. M.; Kitchin, J. R.; Rossmeisl, J. *Chem. Sci.* **2013**, *4*, 1245−1249.
(51) Trotochaud, L.; Ranney, J. K.; Williams, K. N.; Boettcher, S. W. *J. Am. Chem. Soc.* **2012**, *134*, 17253−17261.
(52) De Chialvo, M. R. G.; Chialvo, A. C. *Electrochim. Acta* **1993**, *38*, 2247−2252.
(53) Wu, G.; Li, N.; Zhou, D.-R.; Mitsuo, K.; Xu, B.-Q. *J. Solid State Chem.* **2004**, *177*, 3682−3692.
(54) Mockenhaupt, C.; Zeiske, T.; Lutz, H. D. *J. Mol. Struct.* **1998**, *443*, 191−196.
(55) Pourbaix, M. *Atlas d'Equilibres Electrochimiques*; Gauthiers-Villars: Paris, 1963.
(56) Kondrashev, Y.; Fedorova, N. *Dok. Akad. Nauk SSSR* **1954**, *94*, 229−231.
(57) Delaplane, R. G. *J. Chem. Phys.* **1969**, *50*, 1920.
(58) Hem, J. D.; Roberson, C. E.; Lind, C. J. *Geochim. Cosmochim. Acta* **1985**, *49*, 801−810.
(59) Sasaki, S.; Fujino, K.; Takeuchi, Y. *Proc. Jpn. Acad., Ser. B* **1979**, *55*, 43−48.
(60) *CRC Handbook of Chemistry and Physics*, 93rd ed.; CRC Press: Boca Raton, FL, 2012.
(61) Smith, W. L.; Hobson, A. D. *Acta Crystallogr., Sect. B* **1973**, *29*, 362−363.
(62) Amatucci, G. G.; Tarascon, J. M.; Klein, L. C. *J. Electrochem. Soc.* **1996**, *143*, 1114−1123.